



Structural and optical analyses of sol–gel synthesized hafnium-doped barium calcium titanate

JUDE FERNANDEZ¹, B BINDHU^{1,*} , M PRABU² and K Y SANDHYA³

¹Department of Physics, Noorul Islam Centre for Higher Education, Kumaracoil 629180, India

²Department of Nanotechnology, Noorul Islam Centre for Higher Education, Kumaracoil 629180, India

³Department of Chemistry, Indian Institute of Space Science and Technology, Thiruvananthapuram 695547, India

*Author for correspondence (bindhu.krishna80@gmail.com)

MS received 23 June 2021; accepted 14 November 2021

Abstract. Materials that integrate more than one useful property in single- and multi-phase structures are known as multifunctional materials. Most of them fall in the category of ABO_3 perovskite type and in recent times, these materials have attracted considerable attention from engineers and scientists around the globe for electronic devices of the future. Among the perovskites, barium titanate-based structures have emerged at the top for modern research in advanced materials. In this study, polycrystalline $Ba_{0.85}Ca_{0.15}Ti_{(1-x)}Hf_xO_3$, $x = 0.00, 0.05, 0.10, 0.15$, materials were synthesized by sol–gel combustion technique and their optical properties were studied. X-ray diffraction (XRD) confirmed that, $Ba_{0.85}Ca_{0.15}Ti_{(1-x)}Hf_xO_3$ crystallized at 1000°C with tetragonal symmetry having $P4mm$ space group. In addition to XRD, the presence of the tetragonal phase was confirmed using Raman spectroscopy. The crystallite sizes computed using Scherrer equation were found to range from 15 to 18 nm. Fourier transform infrared spectroscopy analysis showed a significant peak at 565 cm^{-1} , confirming the formation of the metal oxide-based ceramics. Ultraviolet-Visible-near-IR spectroscopy of $Ba_{0.85}Ca_{0.15}Ti_{(1-x)}Hf_xO_3$ showed a slight increase in bandgap energy with the increase of Hf^{4+} . Photoluminescence spectra confirmed the composition of three colours (blue, green and red) with the intensity of emission increasing with Hf^{4+} doping.

Keywords. Sol–gel synthesis; optical properties; photoluminescence; hafnium-doped barium calcium titanate; bandgap energy.

1. Introduction

Ferroelectric perovskites like barium titanate ($BaTiO_3$) find applications in the electronic industry due to the outstanding electro-optic and dielectric properties possessed by them [1–4]. Other potential applications of this perovskite include direct use in piezoelectric sensors, transducers, capacitors and infrared detectors [5,6]. Major parameters that influence the properties of ferroelectric perovskites are grain size and the concentration of dopants [7,8]. Therefore, by using various types of dopants, the properties can be modified to a great extent. This tailoring of the properties in $BaTiO_3$ by doping happens through the substitution of dopants in both the Ba and Ti sites or in either of these sites [9,10]. In addition to doping, another factor that can alter the properties of $BaTiO_3$ is the overall microstructure. This in particular is very important for acquiring great optical performances [11]. To control the microstructure and grain morphology, one can try modified methods of ceramic preparation than rely on high temperature classical methods, where the scope of trying a luck with varied conditions is

limited. One approach is to employ a wet synthesis technique like sol–gel combustion [12–15], which can produce ultra-fine materials. In this method of preparation, the parameters that can be tuned to get desired properties are concentrations of starting chemicals, pH and the temperature to be maintained during the synthesis [16].

The ionic radius of barium ion is quite large; therefore, interesting effects are expected with the addition of a dopant like Ca^{2+} into the Ba site of $BaTiO_3$. It has been reported that, this specific substitution moves the transition point towards room temperature, reducing the possibility of unwanted phases in the final material, promoting the formation of a strong tetragonal structure [17,18]. When prepared using sol–gel method, this specific doping can cause dielectric relaxation in the sample [19]. When $y < 0.20$ in $Ba_{1-y}Ca_yTiO_3$, the material crystallized in the tetragonal phase while a new orthorhombic phase was found to coexist with the tetragonal phase when $y > 0.20$ [20]. This shows that there is a restriction of solubility limits in $Ba_{1-y}Ca_yTiO_3$ ceramic system, which is noteworthy because many systems like Sr^{2+} modified $BaTiO_3$, where Sr^{2+} occupies

the Ba site form solid solutions without this limitation [21]. The ferroelectric properties were also found to improve when $0.0 < y < 0.25$ [22]. Recently, exceptional ferroelectric properties comparable to that of lead-based materials used in the past, reported for calcium and zirconium-doped barium titanate having the composition, $\text{Ba}_{0.85}\text{Ca}_{0.15}\text{Ti}_{0.90}\text{Zr}_{0.10}\text{O}_3$, which also had the concentration of Ca^{2+} in the proposed range [23]. In addition to these points, calcium doping also improves the physical properties and stability of piezoelectric properties, making the material system great for various applications in the electronic industry [24]. Therefore, in the present study, Ca^{2+} was used in the Ba site of the material and its composition was fixed at $y = 0.15$ for $\text{Ba}_{1-y}\text{Ca}_y\text{TiO}_3$.

Many dopants like Eu^{3+} , Fe^{3+} , Ga^{3+} , La^{3+} , Nd^{3+} , Zr^{4+} , Nb^{5+} and Ru^{4+} [18,25–29] were used, to study its effects on BaTiO_3 and BaCaTiO_3 especially for improving the optical properties of the materials. When Zr^{4+} is substituted at the Ti site, the phase transition temperature of BaTiO_3 approached closer to room temperature with increasing Zr^{4+} concentration [30,31]. For this behaviour Ca^{2+} and Zr^{2+} co-doped BaTiO_3 received a lot of praise [32,33]. Liu and Ren [23] showed that $\text{Ba}_{0.85}\text{Ca}_{0.15}\text{Ti}_{0.90}\text{Zr}_{0.10}\text{O}_3$ exhibited high saturation polarization and large piezoelectric properties [34]. It was after this discovery, the material composition received a lot of interest from researchers. In this study, to analyse the optical properties of the proposed ceramic, we replace Zr^{4+} with Hf^{4+} since both the ions are chemically alike and hence similar properties are expected. To the best of our knowledge, investigations related to optical properties of hafnium-doped barium titanate or even hafnium-doped barium calcium titanate are rare and has never been prepared using the proposed sol–gel technique.

Anwar *et al* [35] observed a transformation of tetragonal barium titanate into cubic barium titanate and an occurrence of diffuse phase transition with Hf substitution; they suggested that these behaviours were due to the strained regions in barium titanate lattice caused due to Hf doping in the Ti site. Tian *et al* [36] observed a high piezoelectric coefficient and a decrease in Curie temperature in Hf-doped barium titanate prepared by solid-state reaction method. Garbarz-Glos *et al* [37] found very good mechanical properties for Hf-doped barium titanate prepared by ultrasonication, which they attributed towards the dense microstructure of the material. Halder *et al* [38] prepared Hf-doped barium titanate thin films and observed a decrease in dielectric properties and an increase in bandgap energy with increasing Hf concentration. Zhao *et al* [39] found improvement in transition temperatures, high piezoelectric property and a large strain behaviour in Hf-doped barium calcium titanate. Dai *et al* [40] found the existence of a triple-point morphotropic phase boundary separating the rhombohedral, tetragonal and cubic phases for Hf-doped barium calcium titanate, a high piezoelectric coefficient of 572 pC/N and an improvement in transition temperature. Tsai *et al* [41] reported excellent temperature stability, good

ferroelectric and piezoelectric properties in $(\text{Ba}_{0.97}\text{Ca}_{0.03})(\text{Ti}_{0.96}\text{Sn}_{0.04-x}\text{Hf}_x)\text{O}_3$; they attributed these observations to the presence of oxygen vacancies in the material.

From the literature survey, from the few studies related to the effects of Hf doping on the properties of barium titanate and barium calcium titanate, we understand that Hf doping can cause a significant improvement in the mechanical properties, structural stability, temperature stability and ferroelectric properties of barium titanate-based materials. Therefore, to study the effects of Hf on the optical properties of sol–gel-synthesized barium calcium titanate becomes quite interesting.

In this article, we report the structural and optical properties of $\text{Ba}_{0.85}\text{Ca}_{0.15}\text{Ti}_{(1-x)}\text{Hf}_x\text{O}_3$, $x = 0.00, 0.05, 0.10, 0.15$ materials, prepared using sol–gel synthesis. Besides optical studies, the thermal decomposition behaviour of the as-prepared $\text{Ba}_{0.85}\text{Ca}_{0.15}\text{Ti}_{0.90}\text{Hf}_{0.10}\text{O}_3$ powder is also presented here.

2. Experimental

2.1 Materials

Citric acid anhydrous (99.5%), barium nitrate (99.0%), calcium nitrate tetrahydrate (99.0%) and titanium isopropoxide (99.0%) were acquired from Sisco Research Laboratories Pvt. Ltd. Hafnium dichloride oxide octahydrate (99.9%) and nitric acid (69.0%) were purchased from Alfa Aesar and Merck, respectively.

2.2 Preparation

$\text{Ba}_{0.85}\text{Ca}_{0.15}\text{TiO}_3$ (BCTH0), $\text{Ba}_{0.85}\text{Ca}_{0.15}\text{Ti}_{0.95}\text{Hf}_{0.05}\text{O}_3$ (BCTH5), $\text{Ba}_{0.85}\text{Ca}_{0.15}\text{Ti}_{0.90}\text{Hf}_{0.10}\text{O}_3$ (BCTH10) and $\text{Ba}_{0.85}\text{Ca}_{0.15}\text{Ti}_{0.85}\text{Hf}_{0.15}\text{O}_3$ (BCTH15) ceramics were synthesized via a wet-chemical method known as sol–gel. By using a mixer, citric acid was first stirred in de-ionized (DI) water, until completely dissolved. Titanium isopropoxide is now added to the solution along with barium nitrate. It was then followed by the addition of hafnium dichloride oxide octahydrate and calcium nitrate tetrahydrate. Nitric acid was added slowly to maintain the pH of the solution at 1. The solution is stirred at a constant temperature of 100°C. The solution would froth before turning into a dark brown powder after 4 h. The as-prepared powders were calcinated in a high-temperature muffle furnace at 1000°C to remove unwanted compounds and other impurities.

2.3 Characterization

The crystal structures of the sintered ceramics were studied by X-ray diffraction (XRD) using a Bruker D2 Phaser Benchtop diffractometer with Cu K_α radiation (wavelength: 1.54 Å). SII Nano Technology Exstar 6300

thermogravimetric/differential thermal analyser was used to study the thermal decomposition behaviour of as-prepared powder from 0 to 1200°C. Bruker Alpha II Fourier transform infrared spectrophotometer was used for detecting the presence of vibrational groups in the powder. The FTIR (Fourier transform infrared) spectrum was recorded from 500 to 4000 cm^{-1} . EnWAVE EzRaman-N-Analyzer Raman Spectrophotometer was used to assess the structural phases in the material. To assess the microstructure of all the calcinated powders, FEI Apreo LoVac field emission scanning electron microscope (FE-SEM) was used. An Oxford instruments energy-dispersive X-ray analyser was utilized to find the chemical composition of the ceramic. With a Jasco UV-670 V-VIS-NIR spectrophotometer, the absorption spectra of the ceramic powders in the wavelength range 200–800 nm was measured. Using a Jasco FP-8500 fluorescence spectrophotometer, the photoluminescence (PL) spectra of the calcinated powders were recorded at room temperature.

3. Results and discussion

3.1 Structural and morphological studies

X-ray diffraction patterns of BCTH (0, 5, 10 and 15) ceramics calcinated at 1000°C are shown in figure 1. The prepared calcinated powders display a tetragonal phase (JCPDS COD ID: COD 96-150-7758) with the $P4mm$ space group. From the patterns it is evident that the dopants have occupied the respective lattice sites of barium titanate. A pure perovskite structure with secondary phases of BaCO_3 coexisting with the ceramics is obtained. The structure recorded is similar to those obtained in previous reports [42,43]. The average crystallite sizes of BCTH materials were calculated based on the XRD patterns, using Scherrer's equation [44]:

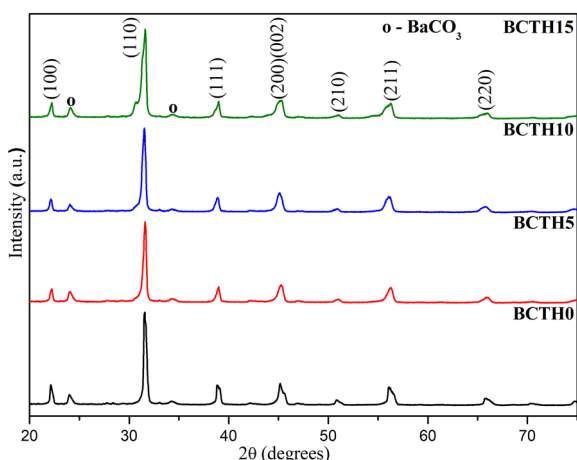


Figure 1. XRD patterns of BCTH (0, 5, 10 and 15) at room temperature.

$$\tau = \frac{0.9\lambda}{\beta \cos \theta}. \quad (1)$$

In the above equation, λ is the wavelength of X-ray, which is 1.5406 Å and the full-width half-maximum is denoted by β . Lastly, θ is the Bragg diffraction angle and τ is the crystallite size. The crystallite sizes calculated for BCTH (0, 5, 10 and 15) are summarized in table 1. The lattice parameters, $a = b$ and c were obtained using the following equation [45]:

$$\frac{1}{d^2} = \frac{h^2 + k^2}{a^2} + \frac{l^2}{c^2}, \quad (2)$$

where, d is the interplanar distance and the values of h , k and l can be obtained from the XRD data. The values obtained for lattice parameters $a = b$ and c along with calculated cell volumes and tetragonality are given in table 1. The variation of lattice parameters with concentration of Hf is shown in figure 2, and the change in cell volume and tetragonality with concentration of Hf is shown in figure 3. The micro-strain, ε , induced in the material due to doping was estimated using the formula [46]:

$$\varepsilon = \frac{\beta \cos \theta}{4}. \quad (3)$$

The dislocation density, δ , of all the samples was calculated using the equation [47]:

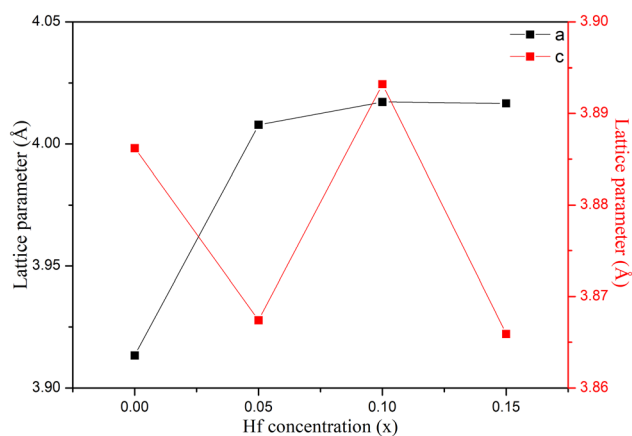
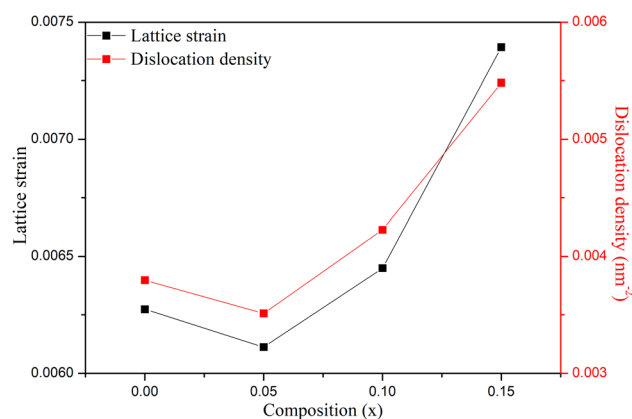
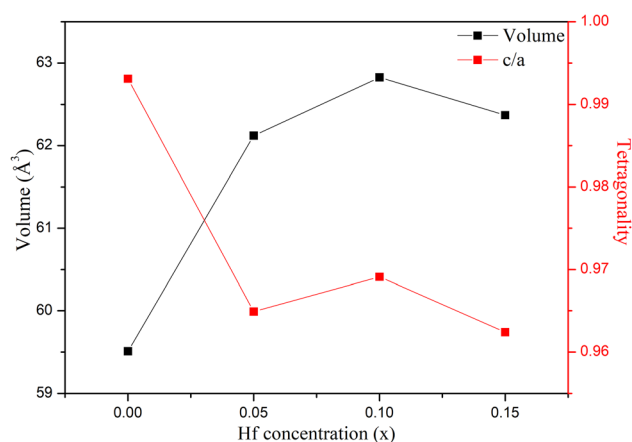
$$\delta = \frac{1}{\tau^2}, \quad (4)$$

where, τ is the crystallite size calculated using Scherrer's equation.

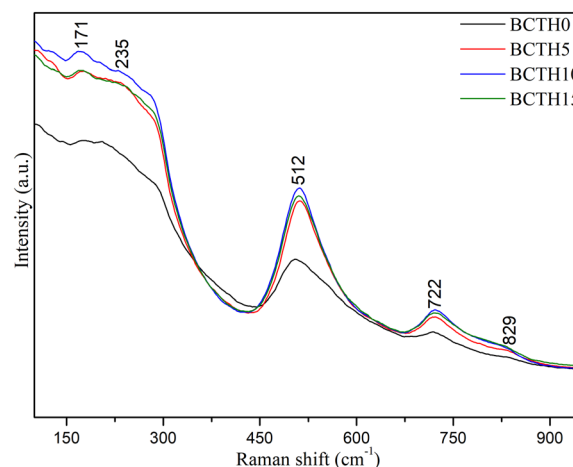
As can be observed from table 1, the lattice parameter a increases and c decreases for BCTH5 when compared to BCTH0, suggesting the substitution of the dopant Hf in the lattice. With further addition of Hf for BCTH10, the lattice parameter a increases, and the parameter c increase and attained a value closer to that of BCTH0. For BCTH15, both the parameters a and c were found to decrease when compared to BCTH10. When it comes to tetragonality, BCTH0 showed the maximum value, while BCTH15 showed the least. The tetragonality of BCTH10 was however better than BCTH5 and BCTH15. The average crystallite size estimated using Scherrer's equation was found to increase to 18.1262 nm for BCTH5 from 17.5005 nm of BCTH0, and with further increase in Hf concentration, the crystallite size reduced to 16.4896 and 15.0757 nm for BCTH10 and BCTH15, respectively. The values obtained are smaller than those estimated by other researchers [48]. The observed changes in lattice parameters and crystallite sizes can be explained as a result of changes in ionic radii between the replacing and replaced elements in the lattice structure [49]. Usually, the introduction of a dopant in a lattice structure, either causes an expansion or a contraction of the unit cell in addition to causing other defects like creation of oxygen vacancies and local electric fields [50].

Table 1. Lattice parameters and crystallite sizes of BCTH (0, 5, 10 and 15).

Composition	Lattice parameters				Crystallite size, D (nm)	Lattice strain, ε	Dislocation density, δ (nm^{-2})
	$a = b$ (\AA)	c (\AA)	V (\AA^3)	c/a			
BCTH0	3.9132	3.8862	59.5099	0.9931	17.5005	0.006273	0.003796
BCTH5	4.0078	3.8674	62.1199	0.9649	18.1262	0.006111	0.003511
BCTH10	4.0172	3.8932	62.8280	0.9691	16.4896	0.006449	0.004226
BCTH15	4.0166	3.8659	62.3688	0.9624	15.0757	0.007393	0.005483

**Figure 2.** Variation of lattice parameters with increasing concentration of Hf.**Figure 4.** Variation of lattice strain and dislocation density with increasing Hf concentration.**Figure 3.** Variation of unit cell volume and tetragonality with increasing Hf concentration.

The unit cell volume was also found to increase with Hf concentration. An important factor that can affect the crystallite size and lattice parameters in general, is the strain induced in the crystal due to doping. To analyse this, the values of induced strain were calculated and presented in table 1. Also, the plot between the concentration of Hf and induced strain is shown in figure 4. The strain caused due to doping was found to increase with increasing Hf concentration and BCTH5 had the least strain among all the doped

**Figure 5.** Raman spectra recorded for BCTH (0, 5, 10 and 15) at room temperature.

samples. An increase in strain causes a contraction of unit cell and further increase causes an expansion. Hence, due to the differences in ionic radii, doping can cause changes in induced strain, an increase or decrease of unit cell size and changes in crystallite sizes [51]. The increase in dislocation density from 0.00379 to 0.00548 nm^{-2} suggests slight decrease in crystallinity of the material with increase in Hf

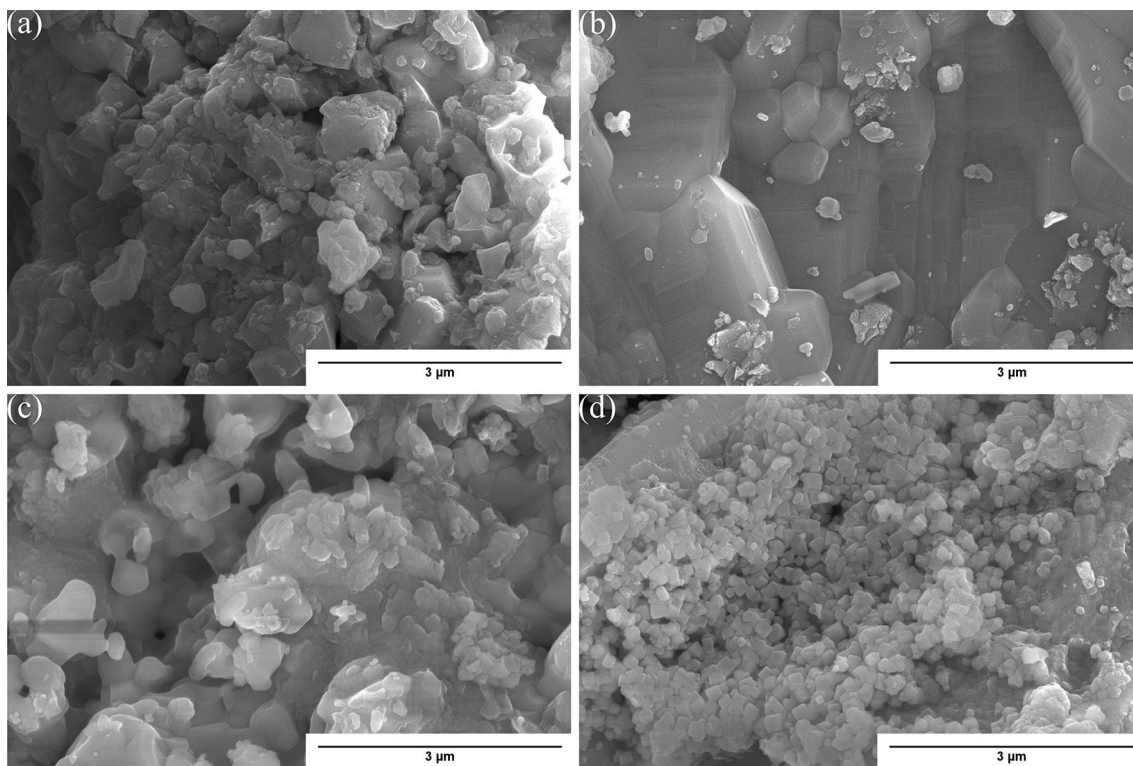


Figure 6. SEM micrographs of (a) BCTH0, (b) BCTH5, (c) BCTH10 and (d) BCTH15.

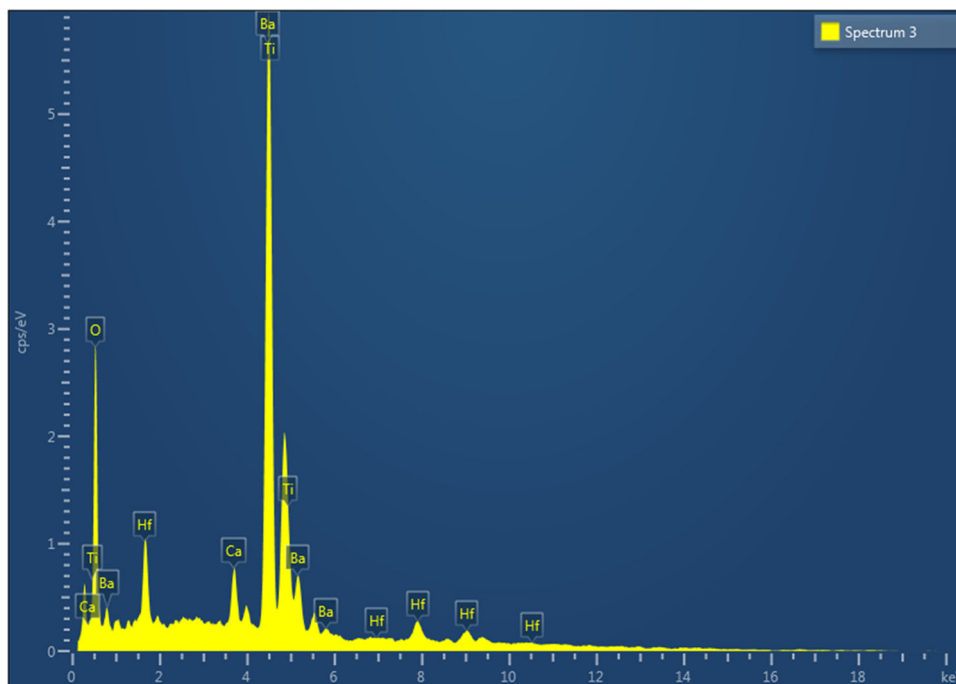


Figure 7. Energy-dispersive X-ray pattern of BCTH10.

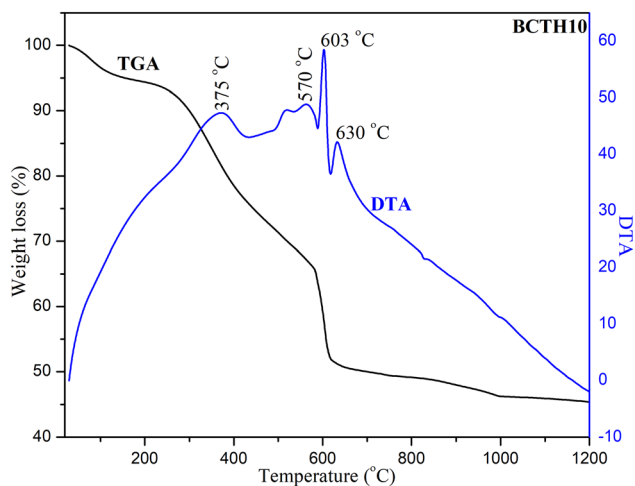
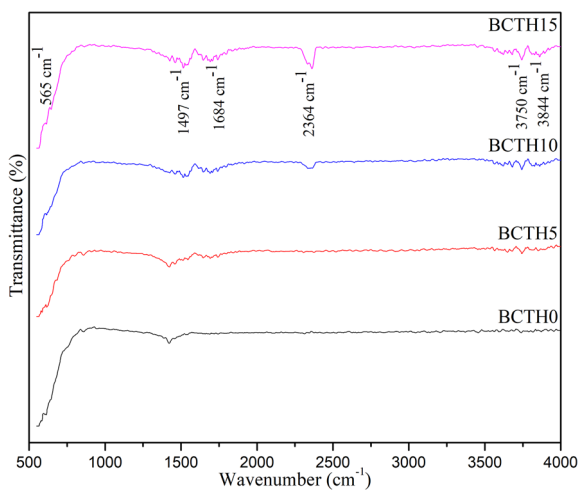
concentration. The plot between dislocation density and concentration of Hf is shown in figure 4, and the corresponding values are also presented in table 1.

Figure 5 shows the room temperature Raman spectra of BCTH (0, 5, 10 and 15) recorded in the range of 100–950

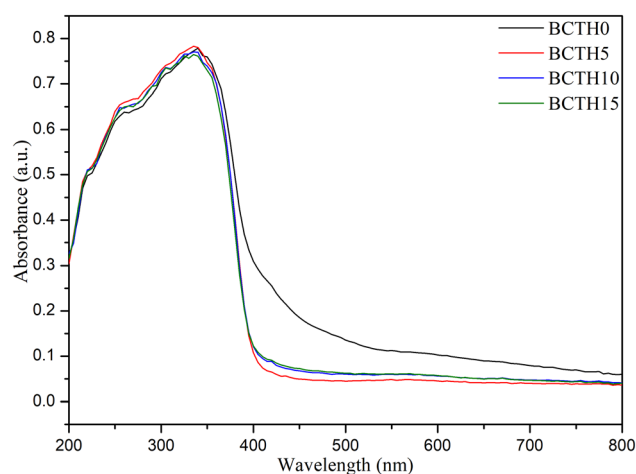
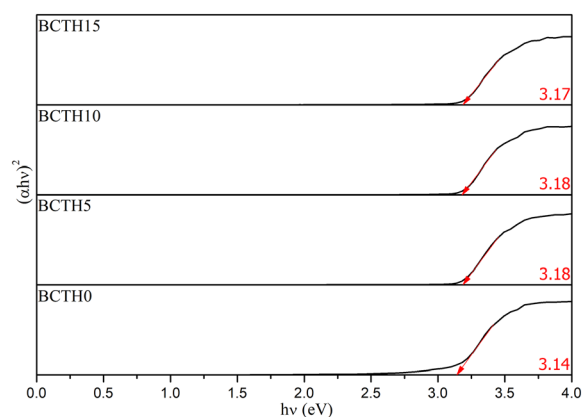
cm^{-1} . This was carried out to find out the presence of multiple phases in the ceramics. Raman spectroscopy is more precise at structure determination and has a lower timescale compared to XRD. Raman peaks are observed at 171, 235, 512, 722 and 829 cm^{-1} . Most of the peaks

Table 2. Elemental composition of $\text{Ba}_{0.85}\text{Ca}_{0.15}\text{Ti}_{0.90}\text{Hf}_{0.10}\text{O}_3$ ceramic

Element	Weight (%)	Atomic (%)
O	3.78	59.45
Ca	0.4	2.51
Ti	3.11	16.32
Ba	10.45	19.13
Hf	1.83	2.58

**Figure 8.** Thermogravimetric/differential thermal analyser analysis of BCTH10 as-prepared powder.**Figure 9.** FTIR spectra of BCTH (0, 5, 10 and 15).

obtained can be related with the tetragonal phase of the material. The observed results are in good agreement with earlier reports [52–57]. The band observed at 171 cm^{-1} [$A_1(\text{TO})$] is weak and its presence may be due to the doping with Hf^{4+} . This weak band is found in tetragonal barium titanate according to some reports [58]. This band can be

**Figure 10.** Absorbance spectra of BCTH (0, 5, 10 and 15).**Figure 11.** Plot of $(\alpha h\nu)^2$ as a function of photon energy for BCTH (0, 5, 10 and 15).

ascribed to asymmetric Ti–O phonon vibrations and are found to shift towards higher frequency region for BCTH5 due to the shrinkage of the unit cell caused due to doping with Hf, which has a larger ionic radius than Ti. However, for BCTH15, the peak shifts marginally towards lower wavenumbers compared to BCTH10; this minor shift is caused due to defects and the strain induced in the lattice as a result of increased dopant concentration. The peaks obtained at 235 cm^{-1} [$A_1(\text{TO})$], 512 cm^{-1} [$A_1(\text{TO})$, $E(\text{TO})$] and 722 cm^{-1} [$A_1(\text{LO})$, $E(\text{LO})$] are strong characteristics of the tetragonal phase [19,59]. The peak at 722 and 512 cm^{-1} observed for all the compositions is caused due to asymmetric vibrations of Ba–O bond, confirming the formation of the tetragonal structure [56]. The peak at 235 cm^{-1} is related to phonon vibrations of Ti–O bonds [50]. Moreover, the broad peaks at 829 cm^{-1} [A_1g] can be further attributed to the presence of atoms, which are not similar in the corresponding sites [27]. The observation that the A_1g mode is present in all the compositions except for BCTH0, confirms the presence of the dopant, Hf^{4+} .

The field-emission scanning electron microscope (FE-SEM) images of BCTH (0, 5, 10 and 15) powders

synthesized using sol–gel method and calcinated at 1000°C are shown in figure 6. As can be observed from the images, the grain geometries appear to be polyhedral, the grains are dense and have round edges. The size of the grains increases for BCTH5 when compared to BCTH0 and then decrease with further increase in Hf^{4+} concentration. The grain sizes for BCTH15 are clearly smaller in the image. The respective average grain sizes of BCTH0, BCTH5, BCTH10 and BCTH15 are 180, 327, 214 and 150 nm. Decreasing grain sizes with increase in dopant concentration is a characteristic feature of ABO_3 -type perovskites. This decrease of grain size can be attributed to the differences in ionic radii between replacing and replaced ions. These differences as observed in the XRD results induces strain effects or stress fields in the crystal, which affect grain growth. This results in decreasing grain size in barium titanate-based perovskites [60]. In figure 7, energy-dispersive X-ray spectrum of BCTH10 is shown. The presence of the elements Ba, Ca, Ti, Hf and O are clearly indicated through the formation of their characteristic peaks, and their elemental composition is given in table 2. So, it can be inferred from the results that the material is free from impurities and all the expected elements of the ceramic are present.

The thermal decomposition behaviour of the precursor gel of BCTH10 at $20^\circ\text{C min}^{-1}$ analysed using thermogravimetric/differential thermal analyser is shown in figure 8. As portrayed in the figure, the curve presents more than one peak for both endothermic and exothermic effects. As a direct consequence of the probable removal of water or dehydration, the differential thermal analysis curve shows an exothermic peak at 375°C leading to a weight loss of around 13%. The peaks at 500, 570, 603 and 630°C , due to the decomposition of metal complex, removal of organic compounds like titanium isopropoxide and citric acid besides the energy utilized for phase formation, resulted to a further weight loss of 37%. Since there is a straight line in the thermogravimetric curve after

630°C , the weight loss after this is negligible and marks the beginning of the perovskite crystallization process. The broad peak in the differential thermal analysis curve at this point is due to the exothermic reaction of remaining carbonates and oxides like HfO_2 and BaCO_3 along with TiO_2 , which aids the formation of the perovskite phase. Although the phase formation starts at a very low 590°C , at around $950\text{--}1000^\circ\text{C}$ where the material in this study was processed, complete phase purity is observed as confirmed by XRD and this is much lower than conventional ceramic processing temperature requirements [61].

3.2 Optical studies

3.2a FTIR analysis: Fourier transform infrared spectroscopy, a valuable aid in assessing the relation between the internal structure and physical properties of a material was put to good use in this study. Figure 9 shows the FTIR spectra of BCTH (0, 5, 10 and 15) ceramics. A broad peak observed at 565 cm^{-1} confirms the existence of the required perovskite metal oxide [61]. A small shift in wavenumber when compared with existing literature is probably due to the incorporation of Ca^{2+} in the BaTiO_3 lattice. The presence of Ti–O and Hf–O stretching vibrations is also confirmed by the peak at 565 cm^{-1} [62,63]. The peaks at 2364 cm^{-1} for BCTH10 and BCTH15 compositions are due to carbon dioxide, which may have evolved as a direct consequence of IR recording conditions. The BCTH0 curve has no peak at 1684 cm^{-1} , while BCTH5, BCTH10 and BCTH15 displays new peaks at these positions. The peaks are believed to have occurred due to the presence of small amounts of C=O carbonyl group formed during the synthesis as a result of decomposition of the alkoxide compound, hafnium dichloride oxide octahydrate [64]. The peaks at 3750 and 3884 cm^{-1} are due to O–H stretching vibrations of absorbed water molecules in the ceramic. The intensity of these peaks increases as Hf^{4+} concentration increases. Therefore, an important observation here is that the hygroscopic nature of the ceramics also increases marginally with increase in Hf concentration.

3.2b Absorbance spectra: In figure 10, the UV–visible absorbance spectra of BCTH (0, 5, 10 and 15) ceramics recorded in the range 200–800 nm are shown. Increase in the absorbance of the sample is clearly seen from 200 nm to approximately 335 nm for all the samples, after which it starts to decrease abruptly. The value of maximum absorbance wavelength increases slightly for BCTH5 when compared with BCTH0 and with further addition of Hf^{4+} , the value starts to decrease. However, the change in the values is moderate.

The bandgap energy of BCTH (0, 5, 10 and 15) ceramics measured using Tauc plot method is shown in figure 11.

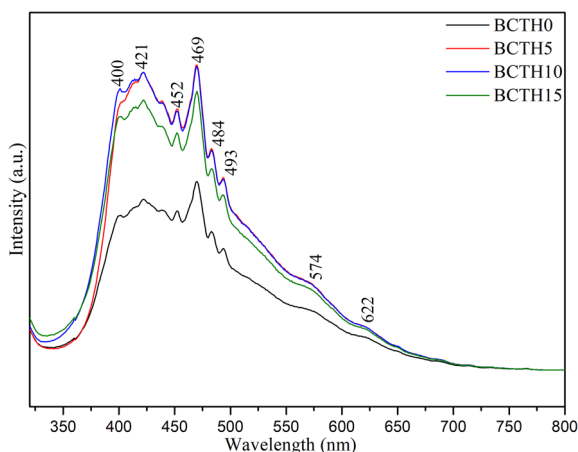


Figure 12. Photoluminescence spectra for BCTH (0, 5, 10 and 15).

From the plotted relationship, the value of bandgap for each sample is found out by extrapolating the linear part of the graph to the photon energy intercept in the x -axis. The values for BCTH0, BCTH5, BCTH10 and BCTH15 were measured as 3.14, 3.18, 3.18 and 3.17, respectively. Hf^{4+} doping slightly increases the bandgap of barium calcium titanate for the compositions, BCTH5 and BCTH10. The reason for the increase in bandgap of BCTH materials with Hf addition is due to different values of electronegativity possessed by the dopant and replacing ions. Bandgap also vary when defects arise in the crystal with increasing dopant concentration. For BCTH15, although similar, the value shows an inappreciable decrease. Therefore, it can be concluded that Hf^{4+} does not alter the bandgap of barium calcium titanate by a large extent.

3.2c Photoluminescence: Photoluminescence (PL) spectroscopy is one of the most important methods for studying the energy levels within the bandgap to observe the extent of disorders in the structure of a material. The phenomenon happens as a result of incident photons and hence the name, photoluminescence. It often occurs in perovskites as a result of self-trapped excitons, existence of polarized states and oxygen vacancies [65].

Considering the structure of barium titanate, we know of various defects associated with its structure, such as nature of surface states, oxygen vacancies and OH^- defects [66]. These together with an occurrence of a charge transfer from a non-centrosymmetric ion, titanium to nearby oxygen ions contributes towards PL in barium titanate-based materials. From the XRD results, it was found that small amounts of phases related to barium carbonate are also present in BCTH. Although barium carbonate does not show PL emission, its presence can cause a slight disorder in the structure of BCTH disturbing the charge transfer from central Ti^{3+} ion to neighbouring O^{2-} ion. In these compounds, the emission occurs due to transitions from $5\text{D}_0 \rightarrow 7\text{F}_j$ ($j = 0, 1, 2, 3, 4$). The PL spectra of BCTH (0, 5, 10 and 15), excited at 300 nm are shown in figure 12. The PL spectra recorded in the range 300–800 nm shows the presence of multiple peaks for BCTH from 400 to 500 nm. The peak centred at around approximately 421 nm occurred due to strong violet emission in the visible region. The peak at 452 nm along with other peaks found at 469, 484 and 493 nm are primarily due to strong blue emissions. The broad yet weak peak observed at 574 nm can be attributed towards green light emission. A further broad peak found at 622 nm is due to emission of red light in the visible region [67,68]. With doping, the intensity of the corresponding peaks of BCTH0 appear to have changed. BCTH5 and BCTH10 showed similar but increased intensities of emission as compared to BCTH0 while for BCTH15, the intensity of emission was found to decrease. However, the intensity of emission of BCTH15 was not as weak as BCTH0. Therefore, we can conclude that Hf^{4+} addition in barium calcium titanate results in the increase of intensity in PL emission.

4. Conclusion

To sum up, we have presented a lucid report on the synthesis, structure and optical properties of $\text{Ba}_{0.85}\text{Ca}_{0.15}\text{Ti}_{(1-x)}\text{Hf}_x\text{O}_3$, $x = 0.00, 0.05, 0.10$ and 0.15 . XRD results showed, the ceramics prepared by sol–gel technique exhibited perfect crystallisation, the structure displayed tetragonal symmetry with the P4mm space group and further confirmation for the presence of the tetragonal phase was done using Raman spectroscopy. The crystallite size measured using Scherrer's equation was found to decrease with increasing concentration of Hf^{4+} . Thermogravimetric/differential thermal analyser showed, the phase formation begins from a temperature as low as 590°C , and as confirmed by XRD, complete crystal structure is obtained at around 1000°C with minimal impurity phases. This remark was again further confirmed by FTIR spectroscopy, in which the peak corresponding to the formation of the required metal oxide phase was well observed for the ceramics calcinated at the mentioned temperature. The estimated particle size for the ceramics were found to vary from 150 to 330 nm using FE-SEM analysis. The bandgap energy estimated from the absorbance spectra using the method of Tauc plot analyses increased slightly with the addition of Hf^{4+} . Moreover, the intensity of PL emission composed of blue, green and red colours. These were observed to increase with the addition of Hf^{4+} making the material suitable for opto-electronic applications.

Acknowledgements

We are grateful to the Central Laboratory for Instrumentation and Facilitation (CLIF), University of Kerala, Thiruvananthapuram, India and Sophisticated test and Instrumentation Centre (STIC), Cochin University of Science and Technology, Kochi, India, for providing characterization facilities.

References

- [1] Scott J F 2007 *Appl. Mod. Ferroelectr.* **315** 954
- [2] Huan Y, Wang X, Fang J and Li L 2014 *J. Eur. Ceram. Soc.* **34** 1445
- [3] Upadhyay R H, Argekar A P and Deshmukh R R 2014 *Bull. Mater. Sci.* **37** 481
- [4] Xu Y (ed) 1991 *Ferroelectric materials and their applications* (Amsterdam: Springer)
- [5] Nalwa H S (ed) 1999 *Handbook of low and high dielectric constant materials and their applications* (New York: Academic Press)
- [6] Kishi H, Mizuno Y and Chazono H 2003 *Jpn. J. Appl. Phys.* **42** 1
- [7] Xu J, Menesklou W and Ivers T E 2004 *J. Eur. Ceram. Soc.* **24** 1735

- [8] Lee B I 1999 *J. Electroceram.* **3** 53
- [9] Zheng R K, Wang J, Tang X G, Wang Y, Chan H L W and Choy C L 2005 *J. Appl. Phys.* **98** 084108
- [10] Wang L, Liu L, Xue D, Kang H and Liu C 2007 *J. Alloys Compd.* **440** 78
- [11] Park J S, Lee Y H, Kim K B and Kim Y 2012 *Nucl. Instrum. Methods Phys. Res. Sect. B Beam Interact. Mater. Atoms* **284** 44
- [12] Khort A A and Podbolotov K B 2016 *Ceram. Int.* **42** 15343
- [13] Khedhri M H, Abdelmoula N, Khemakhem H, Douali R and Dubois F 2019 *Appl. Phys. A* **125** 193
- [14] Zhao G, Chen L, Tang Y, He L, Long B, Nie Z and Chen H 2015 *Mater. Sci. Forum* **809** 136
- [15] Zhang M S, Yin Z, Chen Q, Zhang W and Chen W 2001 *Solid State Commun.* **119** 659
- [16] Hernandez M G, Chadeyron G, Boyer D, Murillo A G, Romo F C and Mahiou R 2013 *Nano-Micro Lett.* **5** 57
- [17] Yang Y, Hao H, Zhang L, Chen C, Luo Z, Liu Z *et al* 2018 *Ceram. Int.* **44** 11109
- [18] Jiang X, Hao H, Yang Y, Zhou E, Zhang S, Wei P *et al* 2021 *J. Materiomics* **7** 295
- [19] Salhi A, Sayouri S, Alimoussa A and Kadira L 2019 *Mater. Today Proc.* **13** 1248
- [20] Khedhri M H, Abdelmoula N, Khemakhem H, Douali R and Dubois F 2019 *Appl. Phys. A Mater. Sci. Process.* **125** 193
- [21] Cheng X and Shen M 2007 *Mater. Res. Bull.* **42** 1662
- [22] Rached A, Wederni M A, Khirouni K, Alaya S, Martín-Palma R J and Dhahri J 2021 *Mater. Chem. Phys.* **267** 124600
- [23] Liu W and Ren X 2009 *Phys. Rev. Lett.* **103** 257602
- [24] Motta F V, Marques A P A, Espinosa J W M, Pizani P S, Longo E and Varela J A 2010 *Curr. Appl. Phys.* **10** 16
- [25] Barik P and Kundu T K 2013 *Nanosyst. Phys. Chem. Math.* **4** 269
- [26] Cernea M, Vasilescu C A, Secu M, Aldica G, Surdu A and Ganea P 2016 *J. Mater. Sci. Mater. Electron.* **27** 11371
- [27] Petrovic M M V, Bobic J D, Ramoska T, Banys J and Stojanovic B D 2011 *Mater. Charact.* **62** 1000
- [28] Maso N, Beltran H, Cordoncillo E, Flores A A, Escribano P, Sinclair D C *et al* 2016 *J. Mater. Chem.* **16** 3114
- [29] Sarkar B, Chakrabarti K, Das K and De S K 2012 *Phys. D. Appl. Phys.* **45** 505304
- [30] McQuarrie M and Behnke F W 1954 *J. Am. Ceram. Soc.* **37** 539
- [31] Maiti T, Guo R and Bhalla A S 2008 *J. Am. Ceram. Soc.* **91** 1769
- [32] Hao J, Bai W, Li W and Zhai J 2012 *J. Am. Ceram. Soc.* **95** 1998
- [33] Tian Y, Chao X, Wei L, Liang P and Yang Z 2013 *J. Appl. Phys.* **113** 184107
- [34] Loreto A D, Machado R, Frattini A and Stachiotti M G 2017 *J. Mater. Sci. Mater. Electron.* **28** 588
- [35] Anwar S, Sagdeo P R and Lalla N P 2006 *Solid State Commun.* **138** 331
- [36] Tian H Y, Wang Y, Miao J, Chan H L W and Choy C L 2007 *J. Alloys Compd.* **431** 197
- [37] Garbarz-Glos B, Piekarczyk W, Smeltere I, Smiga W and Antonova M 2012 *Ferroelectrics* **436** 87
- [38] Halder S, Schneller T, Waser R and Majumder S B 2008 *Thin Solid Films* **516** 4970
- [39] Zhao C, Wang H, Xiong J and Wu J 2016 *Dalton Trans.* **45** 6466
- [40] Dai Z, Li D, Xie J, Liu W, Ge S, Zhang J *et al* 2019 *Funct. Mater. Lett.* **12** 1950070
- [41] Tsai C C, Chao W H, Chu S Y, Hong C S, Weng C M and Su H H 2016 *AIP Adv.* **6** 125024
- [42] Zhao C, Wu B, Thong H C and Wu J 2018 *J. Eur. Ceram. Soc.* **38** 5411
- [43] Cullity B D and Stock S R (eds) 2014 *Elements of X-ray diffraction* (Upper Saddle River: Pearson Education Limited)
- [44] Sun Z, Pu Y and Zhang C 2015 *J. Mater. Sci. Mater. Electron.* **26** 1275
- [45] Batoo K M, Raslan E H, Yang Y, Adil S F, Khan M, Imran A *et al* 2019 *AIP Adv.* **9** 055202
- [46] Batoo K M, Kumar G, Yang Y, Al-Douri Y, Singh M, Jotania R B *et al* 2017 *J. Alloys Compd.* **726** 179
- [47] Takuya H 2013 *J. Ceram. Soc.* **121** 156
- [48] Richerson D W and Lee W E (eds) 1992 *Modern ceramic engineering: properties, processing, and use in design* (New York: Taylor & Francis Group)
- [49] Cernea M, Secu M, Radu R, Ganea P, Vasile A S, Surdu V A, Trusca R *et al* 2021 *J. Alloys Compd.* **878** 160380
- [50] Verma R, Chauhan A, Batoo K M, Hadi M, Raslan E H, Kumar R *et al* 2021 *J. Alloys Compd.* **869** 159520
- [51] Sati A, Mishra V, Kumar A, Warshi M K, Sagdeo A, Kumar R *et al* 2019 *J. Mater. Sci. Mater. Electron.* **30** 9498
- [52] Sood A K, Chandrabhas N, Muthu D V S and Jayaraman A 1995 *Phys. Rev. B* **51** 8892
- [53] Pasha U M, Zheng H, Thakur O P, Feteira A, Whittle K R, Sinclair D C *et al* 2007 *Appl. Phys. Lett.* **91** 062908
- [54] Khalid M B, Ritesh V, Ankush C, Rajesh K, Muhammad H, Omar M A *et al* 2021 *J. Alloys Compd.* **883** 160836
- [55] Sati A, Pokhriyal P, Kumar A, Anwar S, Sagdeo A, Lalla N P *et al* 2021 *J. Phys. Condens. Matter* **33** 165403
- [56] Sun D, Jin X, Liu H, Zhu J, Zhu Y and Zhu Y 2007 *Ferroelectrics* **355** 145
- [57] Perry C H and Hall D B 1965 *Phys. Rev. Lett.* **15** 700
- [58] Abdessalem M B, Aydi A, Abdelmoula N, Sassi Z and Khemakhem H 2017 *Appl. Phys. A* **123** 583
- [59] Puli V S, Kumar A, Chrisey D B, Tomozawa M, Scott J F and Katiyar R S 2011 *J. Phys. D Appl. Phys.* **44** 395403
- [60] Binhyeeniyi N, Sukvisut P, Thanachayanont C and Muensit S 2010 *Mater. Lett.* **64** 305
- [61] Zak A K, Majid W H A, Abrishami M E and Yousefi R 2011 *Solid State Sci.* **13** 251
- [62] Rached A, Wederni M A, Khirouni K, Alaya S, Palma R J M and Dhahri J 2021 *Mater. Chem. Phys.* **267** 124600
- [63] Jin X, Sun D, Zhang M, Zhu Y and Qian J 2009 *J. Electroceram.* **22** 285
- [64] Disalvo E A and Frias M A 2013 *Langmuir* **29** 6969
- [65] Singh A P, Kumar S and Thirumal M 2019 *ACS Omega* **4** 12175
- [66] Zhang M S, Yu J, Chen W and Yin Z 2000 *Prog. Cryst. Growth Charact. Mater.* **40** 33
- [67] Cho W S and Hamada W 1998 *J. Alloys Compd.* **268** 78
- [68] Lu S G, Xu Z K, Chen H, Mak C L, Wong K H, Li K F *et al* 2006 *J. Appl. Phys.* **99** 064103